X-ray magnetic-circular-dichroism study of Ni/Fe (001) multilayers

Tao Lin, M. M. Schwickert, M. A. Tomaz, H. Chen, and G. R. Harp
Department of Physics and Astronomy, Ohio University, Athens, Ohio 45701
(Received 24 July 1998; revised manuscript received 30 November 1998)

The structure and magnetic properties of Fe/Ni(001) multilayers are studied using x-ray diffraction, magneto-optical Kerr effect magnetometry, and x-ray magnetic circular dichroism. Multilayers are deposited with constant Fe layers (12 Å) and wedged Ni layers (0–30 Å), repeated 20 times, to explore the magnetic moment and the structure dependence upon thickness of Ni (t_{Ni}). Up to $t_{\mathrm{Ni}} \approx 16$ Å (11 ML), both the Fe and the Ni have a bct structure, similar to the bulk structure of bcc Fe. The magnetic moments of Ni in the bct region are nearly constant at $0.85\mu_B$ for a Ni thickness t_{Ni} in the range 3 Å$< t_{\mathrm{Ni}} <$16 Å. This represents a significant enhancement over the moment in bulk fcc Ni ($0.59\mu B$). The Fe/Ni multilayer undergoes a crystalline phase transition between 16 Å$< t_{\mathrm{Ni}} <$23 Å, beyond which both the Fe and Ni have an fct structure. In the fct region, the Ni magnetic moment is close to its bulk value and the Fe magnetic moment drops to $1.5\mu_B$, which is ~70% of its bulk value. The crystalline phase transition is also accompanied by a rotation of the magnetic easy axis by 45° in the plane of the film. [S0163-1829(99)13521-5]

I. INTRODUCTION

The magnetic properties of transition metals are known to depend strongly upon their crystal structure. One way to artificially control the structure is through the preparation of superlattices, where a metastable phase of one element may be stabilized through epitaxial growth. Many metastable systems have been achieved which may exhibit unusual properties. For example, substantial magnetic moments can be induced in normally nonmagnetic elements.[1,2]

As an important ferromagnetic metal, the structure and magnetic properties of Ni have been studied in many experiments on thin films and multilayers.[3–18] Specifically, several studies have discussed magnetic moments in metastable bct Ni films on Fe(001).[3,5,7–10,14,15] All of these give results of a reduced magnetic moment for bct Ni as compared to the bulk [e.g., $0.33\mu_B$ for 1 ML and $0.39\mu_B$ for 5 ML (Refs. 14,15)], although some of them predicted that the magnetic moment for bct Ni could be higher than $0.4\mu_B$.[7,9] By comparison, theoretical calculations predict a larger moment for bulk bcc Ni;[19] choosing the lattice constant of bulk bcc Fe, they predict the Ni magnetic moment as $0.54\mu_B$. Moreover, calculations of Ni films on Fe(001) find an enhanced Ni magnetic moment ($0.86\mu_B$ for 1 ML, $0.69\mu_B$ for 2 ML thin films). However, in the latter report the c-axis spacing between the 2 monolayers was chosen to be that for fcc Ni, not bcc Ni. Hence, it is not clear what would be predicted for a 2 ML bcc Ni film, which conceivably could have a higher moment.

To shed more light on the disagreement between experiment and theory, we study epitaxial Fe/Ni(001) multilayers. We find that bct Ni may be stabilized within such multilayers up to ≈16 Å thickness. X-ray magnetic circular dichrosim (XMCD) is applied to probe the element specific magnetic moments. The results indicate bct Ni has an enhanced magnetic moment as compared with its bulk value. A phase transition from bct to fct structure is observed for Ni thickness t_{Ni} greater than 16 Å, beyond which the Ni moment approaches its bulk value. The effect of the crystalline phase on the Fe moments is also studied in these experiments.

II. GROWTH AND STRUCTURAL CHARACTERIZATION

The multilayers were prepared by dc magnetron sputtering at a pressure of 3.2×10^{-3} Torr Ar, with a deposition rate of 1 Å /s. The base pressure of this ultrahigh-vacuum system is $<5\times10^{-10}$ Torr. Some samples were deposited with uniform Ni layers, while others were deposited with wedge-shaped Ni layers to explore Ni thickness dependences in films deposited under identical conditions. This paper focuses mainly on a wedge sample with structure as follows. A 25 Å Cr(001) film was deposited onto an MgO(001) substrate at 600 °C to seed subsequent growth. This was followed by a 300 Å Cr layer at 300 °C which provides a flat bcc template for growth of the multilayer. Then, the structure

$$\mathrm{Fe\ 12\ \text{Å}[Ni\ 0\text{–}30\ \text{Å/Fe}\ \ 12\ \text{Å}]_{20}}$$

was deposited at 170 °C. A final 20 Å Al capping layer was deposited at room temperature and used to protect against oxidation after removal from the growth chamber. Results are also reported for an analogous Fe/Ni multilayer grown on MgO(001)/4 Å Cr at 600 °C/250 Å Ni at 250 °C, which provides an fcc template for subsequent growth. In the following, we shall refer to the former (bcc template) structure unless otherwise specified.

Figure 1 displays x-ray-diffraction (XRD) specular scans from several positions on the wedge. These were taken with a two-circle fixed anode diffractometer using Cu K_α radiation with 1° angular resolution. The x-ray beam on the sample is about 2 mm wide, so that it integrates over a Ni thickness range of ≈1.5 Å at any given point. This introduces a significant broadening of the observed x-ray peaks from the multilayer. The dominant features in all spectra are the MgO(002) peak at 43.1° and the Cr(002) peak at 64.9°. An additional small feature at 54° in all scans is associated with defects in the substrate. The bct Fe/Ni(002) features are visible between 60° and 80° in scans with $t_{\mathrm{Ni}} \leqslant 16$ Å and fct Fe/Ni(002) is visible between 45° and 55° in the scans with $t_{\mathrm{Ni}} \geqslant 20$ Å . This indicates that the Fe/Ni has a coherent superlattice structure before and after the phase transition.

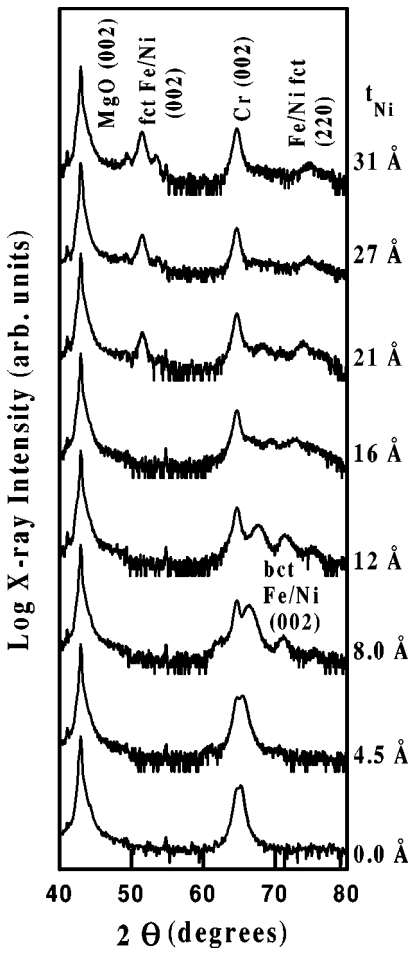

FIG. 1. X-ray-diffraction spectra from Fe 12 Å/Ni t_{Ni} (001) multilayers. The main features observed are the MgO substrate (002) peak at 43° and the Cr seed layer peak at 64.9°. For $t_{Ni} \leq 16$ Å, the multilayer features appear between 60 and 80°, indicating a coherent bct structure. Beyond $t_{Ni}=16$ Å, the main multilayer features appear between 45 and 55°, which indicates an fct structure. In the fct region, a weak broad feature appears near 74° due to a minority component of fct(011) orientation within the film.

Where there is no Ni at the beginning of the sample, the bct feature is close to the expected position of bcc Fe(002) peak, just to the right of the Cr(002) peak. As t_{Ni} increases, this peak moves to a larger θ angle, indicating a decreasing c-axis lattice constant. This is consistent with a bct Ni lattice constant that is smaller than that of Fe. As t_{Ni} increases from 16 to 23 Å the films undergo a crystalline phase transition from bct to fct. At $t_{Ni}=16$ Å, the bct multilayer feature begins to broaden suggesting increasing disorder, but no fct(002) multilayer feature is yet visible. At $t_{Ni}=21$ Å a strong fct Fe/Ni(002) has appeared, coexisting with degraded intensity in the bct region of the spectrum. It was reported that the intermediate Ni phase is a structure consisting of small domains.[18] Finally, for $t_{Ni} \geq 23$ Å the fct crystal structure dominates. Some superlattice satellites are also evident, indicating good quality Fe/Ni layering.

In all spectra for $t_{Ni} \geq 21$ Å, a weak fct(220) feature can be seen near 74°. This represents a minority component within the fcc films, yet it could influence the magnetic properties. For this reason, the second Fe/Ni wedge was prepared

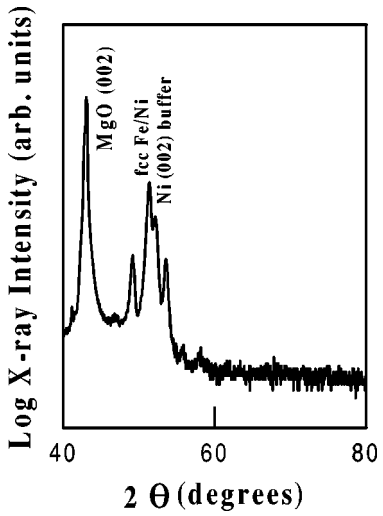

FIG. 2. X-ray-diffraction scan from the fcc-template multilayer with $t_{Ni}=27.75$ Å. This scan shows that this sample is 100% fct(001) oriented with no minority fct(011) component. Otherwise the magnetic and structural properties of this sample are indistinguishable from those of the analogous part of the bcc-template sample (previous figure). From this we conclude that the minority component of fct(011) orientation evident in the previous figure does not strongly affect the macroscopic properties of the bcc-template sample.

using the fcc Ni template. An x-ray spectrum from one position on this sample is presented in Fig. 2. Here it is seen that a single fct(001) orientation was achieved within this sample. As an aside we note that within the bct region the fcc template sample showed a majority bct(110) orientation.

Returning to the bcc template sample, for each position the average perpendicular spacing c was determined from the position of the Fe/Ni(002) peak. This data is plotted in the top panel of Fig. 3. To fully characterize the crystal structure, it is also required to know the in-plane lattice parameter a. This was determined using off-normal radial diffraction scans through the bct(103) feature of all the samples. [Note that this peak is equivalent to the fct(113) when indexed on an fct lattice system. However, for the rest of this discussion, we will index all samples on the bct lattice.] From the bct(103) measurements and c, it is possible to deduce a. The results for a are plotted in the lower panel of Fig. 3. It was not possible to measure the bct(103) feature for $t_{Ni}=16$ Å as it was too weak and broad, so this point is omitted. The best characterization of the lattice structure can be found in the c/a ratio, plotted in the middle panel of Fig. 3. Recall that a perfect bcc lattice has $c/a=1$,while a perfect fcc lattice has $c/a=1.414$. It is seen that for $t_{Ni}<16$ Å, c/a is very close to 1. We interpret this as signifying that the bcc structure must be a very stable local minimum for Ni, since films with equal parts Fe and Ni are almost perfectly bcc. The fact that $c/a<1$ in this region can be understood from the fact that a is set by the Fe template, while c is more free to relax (contract) due to the smaller Ni atomic radius. Likewise, after the phase transformation the lattice is almost perfectly fcc with $c/a=1.40$. This suggests that fcc is a nearly stable structure for Fe, which is well known.

Some samples that are perfectly analogous to the bcc template sample but with uniform Ni layers were prepared to

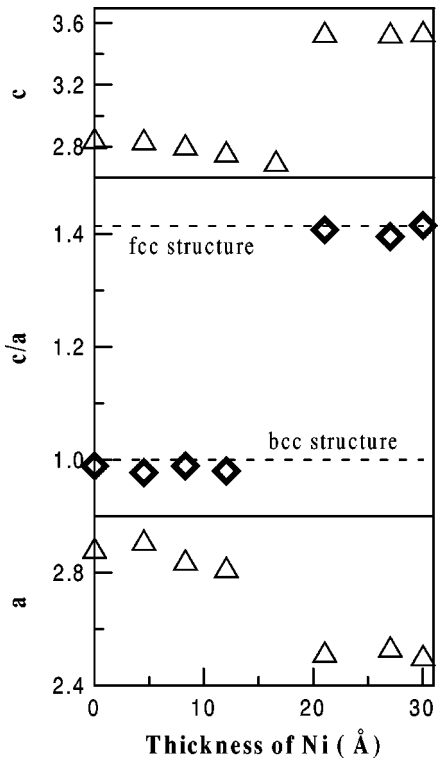

FIG. 3. Top panel: The average perpendicular spacings (c) for different t_{Ni} as determined from the 2θ angle of the Fe/Ni (002) peaks in Fig. 1. Bottom panel: The average in-plane lattice constants (a) for each t_{Ni} were deduced from scans through the Fe/Ni (103) peak (not shown). The ratio c/a (middle panel) is a continuous parameter that allows us to distinguish bcc-like ($c/a \approx 1$) and fcc-like ($c/a \approx 1.414$) regions of the sample. Because the bct(103) feature for $t_{Ni}=16$ Å was too weak and broad for its position to be accurately measured, this point was omitted from the middle and bottom panels.

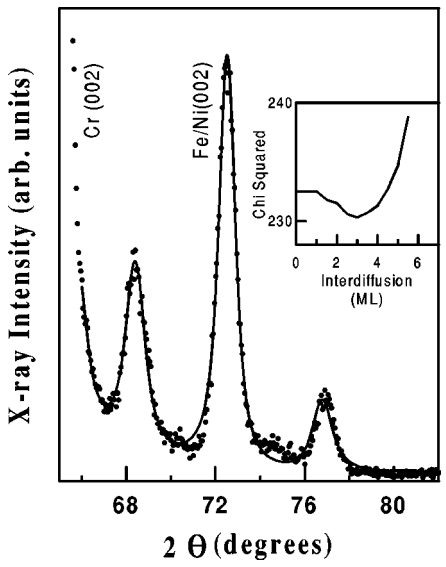

FIG. 4. XRD raw data from a (Fe 10 ML/Ni 10 ML) multilayer (dots) were simulated (solid line) by optimizing the detailed lattice parameters in the Suprex program. The peak on the left side is from the seed layer Cr. The largest peak in the center is the main peak of Fe/Ni(002) multilayers. The two small peaks are the satellite peaks of the multilayers. The c-axis lattice constants determined from this fit were 1.36 and 1.25 Å for Fe and Ni, respectively. The relation between χ^2 and the interdiffusion thickness is shown in the inset. χ^2 is sum of the squared differences between the raw data and the fit. From the curve of χ^2 vs interdiffusion, the best fit is found for an interdiffusion of 3 ML.

evaluate the interdiffusion between Fe and Ni layers. XRD data from these samples were simulated using the Suprex program which can provide the detailed information of lattice parameters and interdiffusion of superlattice sample. The program developed by Fullerton *et al.*[20–22] Figure 4 shows the best fitting of the specular XRD data from one such sample. The multilayer structure was found to be 10 ML Fe/10 ML Ni, with Fe and Ni perpendicular lattice constants of 1.36 and 1.25 Å, respectively. The best fit was obtained with a model including 3 ML of interdiffusion at each interface. The variation of χ^2 with interdiffusion is displayed in the inset. For this graph, the interdiffusion was set at each value in turn, and all the other fitting parameters were allowed to relax to achieve the minimum χ^2.

III. MOKE MEASUREMENTS

The effect of the bct→fct phase transition is clearly observed in the magnetic measurements. Figure 5 shows hysteresis loops for films with different t_{Ni} measured by magneto-optic Kerr effect (MOKE) magnetometry. Notice that the easy axis changes from the bct[100] to the bct[110] direction. A careful analysis of the saturation field shows that this switch occurs at $t_{Ni}=21$ Å, just at the position of the structural phase transition. This means that the first in-plane anisotropy constant has a zero crossing at $t_{Ni}=21$ Å. The same behavior is observed in the fcc template sample, indicating that the anisotropy behavior is not dominated by the minority fct(110) component in the bct template film. A similar zero crossing of the first anisotropy constant is observed in Fe/Pt(001) multilayers.[23]

Figure 6 reveals the relation between t_{Ni} and the saturation longitudinal Kerr effect. From the beginning at $t_{Ni}=0$ Å, the saturation Kerr effect increases smoothly to a peak at $t_{Ni}=16$ Å, and then it falls through the region of the phase transition. After the phase transition, the Kerr effect plateaus. The present films are relatively thick compared to the MOKE sampling depth, hence the MOKE is more a measure of the magnetization density, rather than the total magnetization. In particular, since Ni has a smaller Kerr effect than Fe, one might expect the MOKE effect to decrease with increasing Ni thickness. Surprisingly, this is not observed through the bcc region of the samples. Instead, the MOKE effect increases. Because the Kerr effect is indirectly related to the magnetization, the initial increase is difficult to interpret. It could arise from several factors: (1) an enhancement of the Fe moment; (2) an enhancement of the Fe Kerr rotation due to Fe-Ni hybridization and symmetry breaking at the Fe/Ni interface; and (3) the same effects applied to Ni. The sharp drop near $t_{Ni}=21$ Å strongly suggests a loss of magnetization during the phase transition. However, a change in the matrix elements governing the MOKE effect, caused by the change in symmetry in going from a bct to fct lattice cannot be excluded as cause for this effect. We solve this ambiguity using XMCD below.

Also plotted in the Fig. 6 is the coercivity as a function of

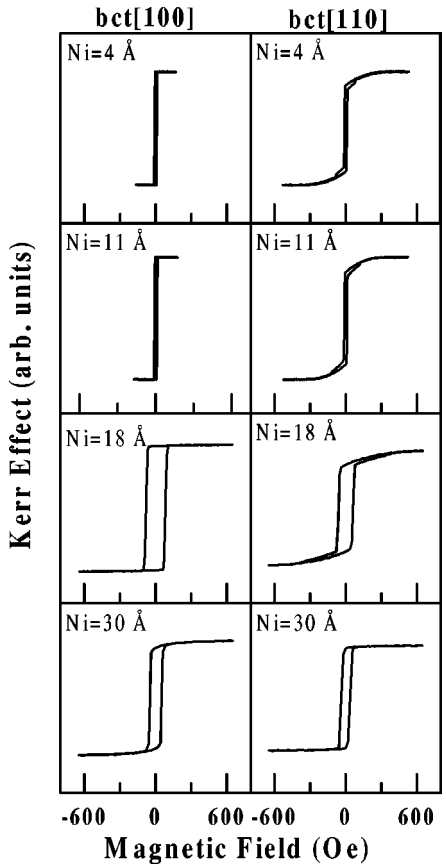

FIG. 5. These hysteresis loops were taken along the bct [100] and bct [110] in plane directions of the sample. All the samples show a fourfold in-plane anisotropy. For $t_{Ni}<21$ Å, we observe that the saturation field is lowest along the [100] direction, making this the easy axis. For $t_{Ni}>21$ Å, the saturation field is lowest along the [110] direction, indicating a switching of the easy axis by 45° in the plane of the film. This shows that the first in-plane anisotropy constant has a zero crossing at $t_{Ni}=21$ Å.

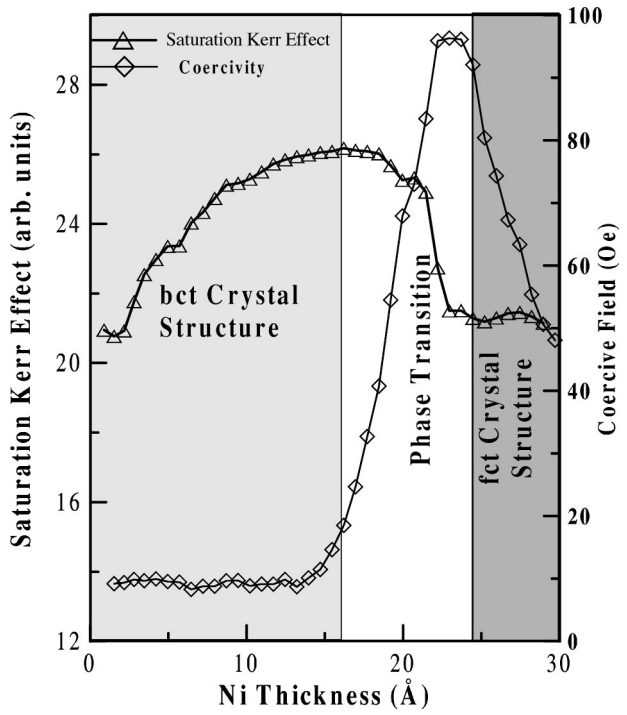

FIG. 6. The magnetic properties obtained from MOKE along the bct[100] axis are summarized in this graph. The saturation Kerr effect, which is roughly proportional to the total magnetic moment, increases gradually with increasing t_{Ni} in the bct region (the lightly filled part) and the coercivity does not change. In the phase-transition region, the saturation Kerr effect decreases rapidly, and the coercive field has a cusp which indicates a high degree of disorder. Finally, in the fct region (the heavily filled part), the Kerr effect stays constant and the coercivity decreases monotonically.

t_{Ni}. The coercive field exhibits a cusp near $t_{Ni}=21$ Å, which is due to the high degree of disorder in the region of the crystalline phase transition. Similar coercivity behavior associated with crystalline phase transitions have also been observed in other systems.[24,1,25,23,26] Interestingly, the peak of the coercivity is located on the right-hand side of the phase-transition region as determined by x-ray diffraction. This may be partly because the magnitude of the magnetocrystalline anisotropy is passing through zero in the vicinity of the phase transition. Since coercivity arises partly from anisotropy, this might shift the coercivity maximum to a region of nonzero anisotropy.

IV. XMCD EXPERIMENT

To determine the element-specific magnetic moments we employ x-ray magnetic circular dichroism (XMCD). This technique was proposed by Erskine and Stern,[27] then realized by Schütz *et al.*[28] The principle of XMCD is to measure differences in the circularly polarized x-ray-absorption spectra depending on the relative orientation between the magnetic moment and photon helicity.

The samples were transported to the Synchrotron Radiation Center in Madison, WI, and pieces of them were inserted into a UHV chamber (base pressure 1×10^{-10} Torr). Samples were magnetized in saturating fields along the easy axis and measured in remanence.

For Fe, XMCD is performed at the 2*p* absorption edge since this probes the 3*d* final states (which carry most of the magnetic moment). A typical Fe XMCD spectrum is displayed in Fig. 7. Here 85% circularly polarized x-rays are incident on the film at 45° angle of incidence. The magnetization is switched at each photon energy by 180° in the sample plane. This generates two absorption spectra, with the magnetic moment either parallel or antiparallel to the projection of the photon helicity into the sample plane. The difference between these two spectra is the XMCD, which is approximately proportional to the Fe magnetic moment. To extract the Fe magnetic moment, the XMCD magnitude is compared with that of a standard sample, in this case, a pure Fe film. Additionally, the Fe XMCD spectra were compared with the spectrum from the part of the bcc template film with $t_{Ni}=0$, yielding identical results.[29] By this method, the Fe moment determined from the spectrum in Fig. 7 is $2.15\mu_B$, that is, this spectrum has the same XMCD intensity as bulk Fe. The statistical errors in this measurement are only a few percent. However, systematic errors may arise from the fact that XMCD is not exactly proportional to the Fe magnetic moment. The systematic errors have been discussed previously[1,30] and are $<20\%$ of the magnetic moment.

XMCD has been measured in Ni also at the 2*p* edge. The XMCD signal of Ni is smaller than that of Fe, but the statis-

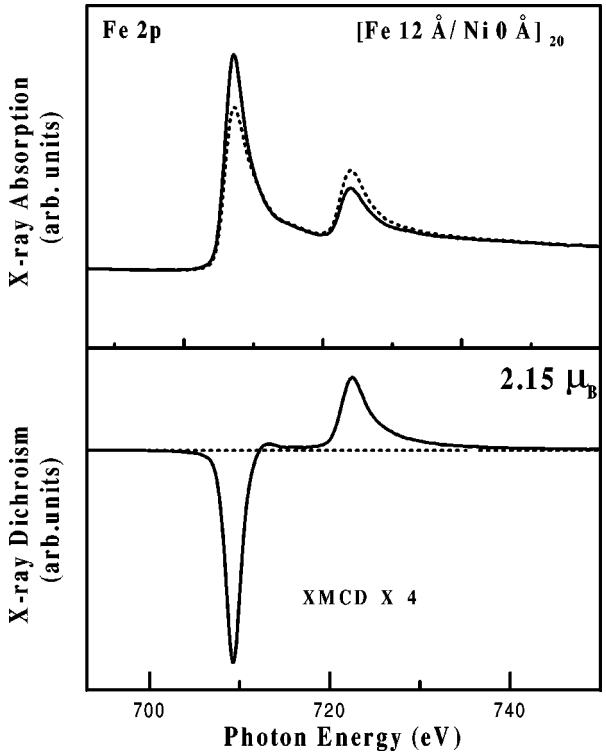

FIG. 7. X-ray absorption spectra (above) near the Fe 2*p* edge. This spectrum was taken at a position on the sample where $t_{\mathrm{Ni}}=0$. As the magnetization direction is switched relative to the photon helicity, two absorption spectra are acquired. The difference of these two spectra is the XMCD (plotted below on an expanded scale). By comparison of the XMCD spectrum with that from a standard sample, we deduce an Fe magnetic moment of $2.15\mu_B$ per atom at this position.

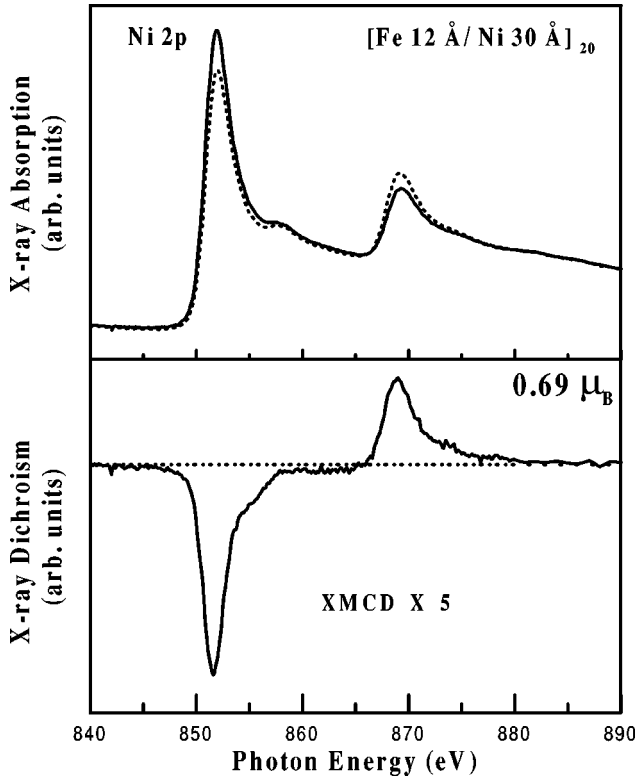

FIG. 8. Typical Ni x-ray absorption spectra (above) and dichroism (below) from another position of the Fe/Ni multilayer as in Fig. 7. Here $t_{\mathrm{Ni}}=29.7$ Å. By a similar procedure, we deduce a Ni magnetic moment of $0.69\mu_B$ per atom in this part of the sample.

tical errors from the measurement are still only a few percent. A standard Ni film was prepared, but it showed an XMCD signal only 75% as large as has been reported by other groups previously for Ni.[31,32] This reduced moment might have been caused by an undesired interaction between the Ni film and Al capping layer. (Note that in previous studies, we have always found the Al capping layer to be inert with respect to the magnetic properties of Fe or Co.) For this reason, we took our standard Ni XMCD spectrum from previously published literature.[31,32] As a check, we also compared Ni spectra to that from a bulk Co film using the transferability approximation,[33] which gave identical results. Figure 8 shows one Ni 2*p* XMCD spectrum. From the XMCD we estimate the Ni magnetic moment at $\approx 0.69\mu_B$ per atom within this sample.

An example of the Ni spectra comparison procedure is shown in Fig. 9. Here the ''unknown'' and ''standard'' spectra were taken from the bcc template sample at positions with $t_{\mathrm{Ni}}=3$ and 30 Å, respectively. At first, the absorption spectra from the two magnetization directions are summed and compared for the two samples. Although they originally appear quite different (top panel), the absorption spectra agree very well after the unknown spectrum has been scaled with a constant and summed with a low-order polynomial background function (middle panel). In most cases, a linear background function is sufficient to achieve good agreement, although occasionally up to third-order polynomial backgrounds are used. The scaling factor and background functions are chosen to achieve the best fit between the two absorption spectra. Then the difference of the standard and scaled unknown absorption spectra for the two magnetization directions is formed (the XMCD, also plotted in the middle panel). Note that the background function applied to compare absorption spectra cancels out from the unknown XMCD spectrum. In the middle panel of Fig. 9, it is seen that the XMCD from the standard is slightly smaller than that in the unknown. The standard is multiplied by a constant factor (here 1.19) to achieve a best fit with the unknown spectrum (shown in lower panel of Fig. 9). From this the magnetic moment per Ni atom in the unknown sample is determined to be 1.19 times as large as the moment in the standard. The same procedure was also applied to determine Fe magnetic moments.

V. ELEMENT-SPECIFIC MAGNETIC MOMENTS

The Fe moments as measured by XMCD are summarized in Fig. 10. In the bct region, the Fe XMCD is enhanced by $\approx 10\%$ over that of bulk Fe. We must be cautious in assigning this enhancement to an increased Fe magnetic moment due to the systematic errors mentioned above. However, an increased Fe moment of similar magnitude was predicted within the calculations of Lee *et al.*[34] Through the phase transition the Fe moment drops by nearly 40%, and stabilizes at $\approx 1.5\mu_B$ in the fct region. This is only 70% of the bulk Fe moment. It is well known that the magnetic moment in fct Fe is strongly dependent on the lattice constant, and ferromag-

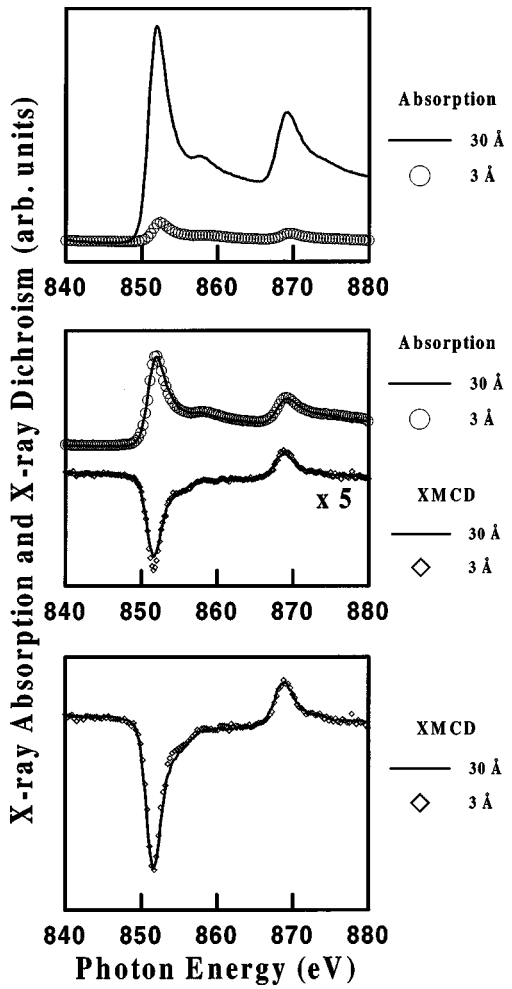

FIG. 9. X-ray-absorption and dichroism spectra comparison procedure: (1) The original absorption spectra are shown in the upper panel (sum of spectra from two magnetization directions). The solid line is the standard spectrum (the spectrum with $t_{\mathrm{Ni}}=30$ Å) and the circles are the unknown spectrum (the spectrum with $t_{\mathrm{Ni}}=3$ Å). To aid in visual clarity, only every third unknown point is plotted. (2) In the middle panel, the unknown spectrum is scaled by a constant factor, and a low-order polynomial background is added to obtain a best fit with the standard absorption spectrum. Also shown in the middle panel are the XMCD spectra (difference of spectra from two magnetization directions) after the processing of the unknown absorption spectra. (3) The bottom panel shows the final result after the standard spectrum is multiplied by a constant (1.19) to achieve the best fit with the unknown spectrum. From this, the magnetic moment per Ni atom in the unknown is determined to be 1.19 times as large as that in the standard.

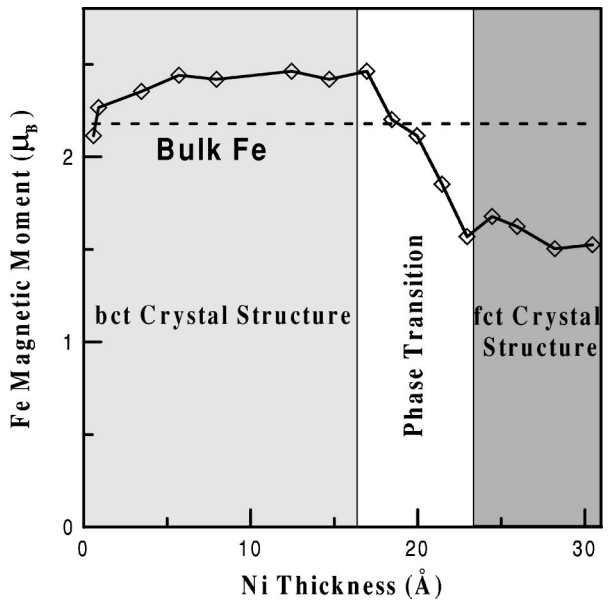

FIG. 10. Summary of the element specific magnetic moments of Fe in Fe/Ni(001) multilayers as measured by XMCD. At the beginning of the curve in which $t_{\mathrm{Ni}}=0$, the magnetic moment is the same as the bulk value of Fe (the dashed line). In the bct region (the lightly filled part), the Fe XMCD is slightly enhanced over its bulk value. The magnetic moments decrease dramatically in the phase-transition region and level off in the fct region at $\approx 70\%$ of the moment in bulk Fe.

netic, antiferromagnetic, and paramagnetic states have all been predicted.[19] Indeed, examples of paramagnetic,[1] ferromagnetic,[23] and antiferromagnetic[35] behaviors are easily found in the literature. The reduced moment ferromagnetic fct state of Fe observed here is similar to that observed in Fe/Pt(001) (Ref. 23) and Fe/Pd(001) (Refs. 36,26) multilayers. However, note that this moment reduction could also arise from a minority component of antiferromagnetic Fe coexisting with ferromagnetic Fe, perhaps in the center of the Fe layer.

Turning now to the Ni moments (Fig. 11), we discern four distinct regions of behavior within this sample. The Ni moment starts at a maximum of $1.1\mu_B$ for $t_{\mathrm{Ni}}=0.5$ Å and decreases rapidly to $\approx 0.85\mu_B$ at $t_{\mathrm{Ni}}=3$ Å. For 3 Å$<t_{\mathrm{Ni}}<$16 Å, the Ni moment is almost constant at $0.85\mu_B$. In the region of the phase transition, the Ni moment decreases, and in the fct region the Ni moment is again constant at $\approx 0.69\mu_B$. In the fct region, one point is plotted showing the Ni magnetic moment within the fcc-template sample. The agreement between the two samples is quite good. We now discuss each of the four regions in turn.

At the beginning of the wedge, interdiffusion plays a dominant role. Since the interdiffused region extends ≈ 3 ML, below $t_{\mathrm{Ni}}=3.75$ Å (3 ML), the multilayers are best regarded as FeNi alloy layers of varying composition separated by pure Fe layers. In this region we may compare the results to Ni moments in bulk FeNi alloys,[37] plotted as a function of composition in Fig. 11. The Ni composition is scaled so that it matches the average composition of the multilayers (infinite interdiffusion). The measured moments are close to those of the alloys in this range. This comparison lends further support to our choice of moment scale for the Ni moments. The comparison with the alloys breaks down rapidly, however, since the invar point (bcc→fcc phase transition) occurs relatively early in the alloys when compared with multilayers having the same average composition. (Note that if the true diffusion profile is used to calculate alloy composition, then the invar point would move to even lower t_{Ni}.)

For thicker films, interdiffusion plays a weaker role. For example, The multilayer with $t_{\mathrm{Ni}}=12$ Å has an approximate profile of [Fe 5.5 ML/FeNi 3 ML/Ni 7 ML/FeNi 3 ML]. According to the linear interdiffusion model used in the Suprex program, these three interdiffused monolayers can be thought of as an alloy with gradually varied concentration: [Fe 83% Ni 17%/ Fe 50% Ni 50%/ Fe 17% Ni 83%]. Thus in

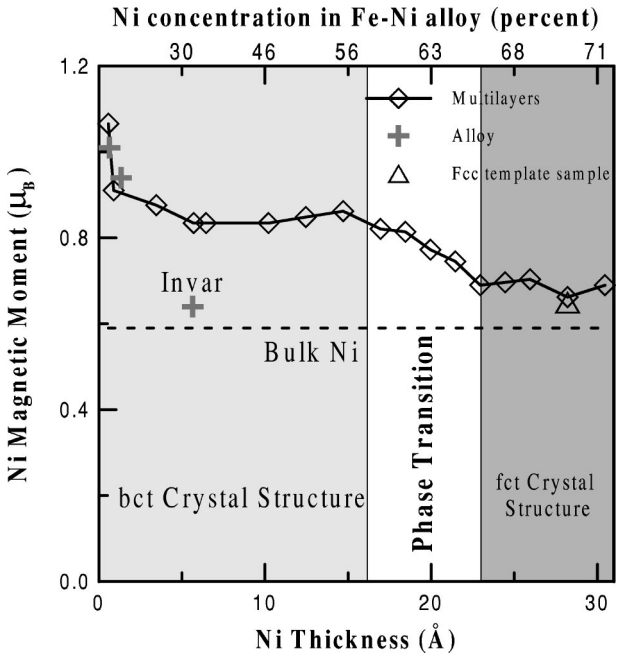

FIG. 11. Summary of the element specific magnetic moments of Ni in Fe/Ni(001) multilayers as measured by XMCD (diamond symbols). Throughout these samples, the measured Ni moments are enhanced above that in bulk fcc Ni (plotted as dashed line), particularly when Ni has a bct structure. For comparison, the Ni magnetic moment in bulk NiFe alloys (gray crosses) are overlaid. Good agreement is achieved between the present results in the interdiffused region ($t_{\mathrm{Ni}}<3$ Å) and the alloy data. However, the body-centered to face-centered phase transition in the alloy (invar point) occurs at a much lower average composition than in the present multilayers. The multilayer Ni moment decreases significantly through the phase-transition region. In the fct region, the Ni magnetic moment stays constant at a level close to the bulk Ni value. Magnetic moment of Ni from the fcc-template multilayer with $t_{\mathrm{Ni}}=27.75$ Å is also presented here (triangle symbol). It gives almost the same value as the bcc-template sample.

the region 3 Å$<t_{\mathrm{Ni}}<$16 Å, there exists an increasing number of Ni atoms which do not have Fe nearest neighbors, while the Ni has a bct structure. In Fig. 11 it is seen that the Ni moment/atom is strongly (and significantly) enhanced above that in fcc Ni throughout this region. This is consistent with the moments predicted in calculations,[34] but in sharp contrast to previous experimental studies where bct Ni showed a reduced moment.[5,14,15] The difference between previous and present experiments is that the Ni films have one vacuum interface, while the Ni multilayers in the present study do not. The reduced coordination of Ni atoms at the vacuum interface might reduce the surface Curie temperature, leading to a suppressed Ni moment. Comparatively, the calculations are performed at 0 K. The suppression of Ni moments in these films is not unlike our fcc Ni film, which displayed a reduced moment possibly due to the Al capping layer. Incidentally, note that if the fcc Ni film had been used as a standard, all the Ni moments in Fig. 11 would be 33% higher.

Beginning at $t_{\mathrm{Ni}}\sim$16 Å, the phase transition is associated with a substantial (20%) decrease in the Ni moments. Yet the decrease in the Ni moment is not as large as that in Fe, which can be understood by consideration of *d*-electron localization.[38] In the transition metals, localization increases with increasing atomic number (within a given row). Thus the Ni *d* electrons are more localized than those of Fe, hence Ni is less sensitive to changes in its local atomic environment. Following the phase transition the Ni magnetic moment is constant in the fct region. The magnetic moment ($0.69\mu_B$) is smaller than in the bct region, but still a little larger than bulk Ni ($0.59\mu_B$). Considering the systematic errors, this enhancement is of borderline significance.

It should be noted that interactions at the Fe/Ni interface are expected to raise the magnetic moment in both Fe and Ni. This can be understood from the ''Slater-Pauling'' curve of magnetic moment vs *d* occupation number in 3*d* transition-metal alloys.[39] There it is seen that a maximal magnetic moment per atom is achieved when the average *d*-band occupation number reaches 7.3 electrons per atom (in this exposition, Fe and Ni are assumed to have 7 and 9 *d*-electrons per atom, respectively). Thus the FeNi alloys developed at the Fe/Ni interface tend to have enhanced Fe and Ni moments, as compared with Fe and Ni atoms in the layer interior. However, it is unlikely that this enhancement could account for the totality of the Ni moment enhancement observed in the bct region. For example, setting $t_{\mathrm{Ni}}=10$ ML, and letting the interior 7 ML have a moment of $0.59\mu_{\mathrm{B}}$, leads to interfacial Ni moments of $1.46\mu_{\mathrm{B}}$, which is not a reasonable value. Although this example is compelling, it should be noted that at the lower limit of the systematic error bar for the Ni moment, the same calculation predicts an interfacial moment of $0.89\mu_{\mathrm{B}}$ which is more reasonable.

In support of the conclusion that the moment enhancement can extend far from the interface, consider studies of Co/Fe multilayers which found that interactions at the Co/Fe interface cause Fe moments enhancements that extend at least 6 ML away from the interface.[40] This is explained as follows: the Fe moments are ''pinned'' to a high value at the interface, although the interior of the Fe layer prefers to have the lower bulk Fe moment. There is an kinetic energy penalty for introducing a ''magnetic interface'' between the high and low moment Fe, because the electron wave function must vary more strongly at the interface than it would if there were no interface. Hence, if the Fe layer is thin enough, the energy gained by lowering the interior moment is not sufficient to warrant introduction of a magnetic interface. At some critical thickness, however, a magnetic interface is created and the interior Fe reverts to the lower moment state. It is reasonable to assume a similar effect is in operation here. Again, the enhanced bcc Ni moment is pinned to a high value at the interface, and this moment enhancement extends several Å into the pure Ni region, as seen in Fig. 11.

VI. CONCLUSION

In conclusion, we have prepared Fe/Ni(001) multilayers and characterized them structurally by XRD and magnetically by MOKE and XMCD. Where the Ni layers are thin ($t_{\mathrm{Ni}}<16$ Å) the multilayers are bct and ferromagnetic, with a nearly constant Fe moment. The average Ni atomic moment is enhanced well above that in fcc Ni. This enhancement is probably due to the reduced coordination of the bct structure and to the interactions at the Fe/Ni interface. Between 16–23 Å, the entire Fe/Ni multilayer suffers a phase transition to an

fct phase. This region is characterized by bulklike Ni moments but depressed Fe magnetic moments.

ACKNOWLEDGMENTS

The authors would like to thank Dr. W. L. O'Brien and Dr. D. Lederman for the valuable conversations. The authors also gratefully acknowledge support of the National Science Foundation CAREER Award No. DMR-9623246. The Synchrotron Radiation Center is supported by NSF under Award No. DMR-953100. The x-ray refinement program was developed with funds provided by the US Department of Energy and the Belgian Interuniversity Attraction Pole Program.

[1] M. A. Tomaz, D. C. Ingram, G. R. Harp, D. Lederman, E. Mayo, and W. L. O'Brien, Phys. Rev. B **56**, 5474 (1997).
[2] M. M. Schwickert, R. Coehoorn, M. A. Tomaz, E. Mayo, D. Lederman, W. L. O'Brien, Tao Lin, and G. R. Harp, Phys. Rev. B **57**, 13 681 (1998).
[3] B. Heinrich, A. S. Arrott, J. F. Cochran, C. Liu, and K. Myrtle, J. Vac. Sci. Technol. A **4**, 1376 (1986).
[4] Z. Q. Wang, Y. S. Li, F. Jona, and P. M. Marcus, Solid State Commun. **61**, 623 (1987).
[5] B. Heinrich, S. T. Purcell, J. R. Dutcher, K. B. Urquhart, J. F. Cochran, and A. S. Arrott, Phys. Rev. B **38**, 12 879 (1988).
[6] C. T. Chen, F. Sette, Y. Ma, and S. Modesti, Phys. Rev. B **42**, 7262 (1990).
[7] J. A. C. Bland, R. D. Bateson, A. D. Johnson, B. Heinrich, Z. Celinski, and H. J. Lauter, J. Magn. Magn. Mater. **93**, 331 (1991).
[8] C. J. Gutierrez, M. D. Wieczorek, Z. Q. Qiu, H. Tang, and J. C. Walker, J. Magn. Magn. Mater. **93**, 369 (1991).
[9] N. B. Brookes, A. Clarke, and P. D. Johnson, Phys. Rev. B **46**, 237 (1992).
[10] Q. M. Zhong, A. S. Arrott, B. Heinrich, and Z. Celinski, J. Magn. Magn. Mater. **104–107**, 1837 (1992).
[11] G. van der Laan, M. A. Hoyland, M. Surman, C. F. J. Flipse, and B. T. Thole, Phys. Rev. Lett. **69**, 3827 (1992).
[12] Hiroshi Sakurai, Fumitake Itoh, Hiroshi Maruyama, Akihisa Koizumi, Kenji Kobayashi, Hitoshi Yamazaki, Yasunori Tanji, and Hiroshi Kawata, J. Phys. Soc. Jpn. **62**, 459 (1993).
[13] M. D. Wieczorek, D. J. Keaveney, D. F. Storm, and J. C. Walker, J. Magn. Magn. Mater. **121**, 34 (1993).
[14] J. Vogel, G. Panaccione, and M. Sacchi, Phys. Rev. B **50**, 5157 (1994).
[15] J. Vogel and M. Sacchi, Phys. Rev. B **53**, 3409 (1996).
[16] P. Srivastava, N. Haack, H. Wende, R. Chauvistré, and K. Baberschke, Phys. Rev. B **56**, R4398 (1997).
[17] F. O. Schumann, R. F. Willis, K. G. Goodman, and J. G. Tobin, Phys. Rev. Lett. **79**, 5166 (1997).
[18] A. V. Mijiritskii, P. J. M. Smulders, V. Ya. Chummanov, O. C. Rogojanu, M. A. James, and D. O. Boerma, Phys. Rev. B **58**, 8960 (1998).
[19] V. L. Moruzzi, P. M. Marcus, K. Schwarz, and P. Mohn, Phys. Rev. B **34**, 1784 (1986).
[20] I. K. Schuller, Phys. Rev. Lett. **44**, 1597 (1980).
[21] W. Sevenhans, M. Gijs, Y. Bruynseraede, H. Homma, and I. K. Schuller, Phys. Rev. B **34**, 5955 (1986).
[22] E. E. Fullerton, I. K. Schuller, H. Vanderstraeten, and Y. Bruynseraede, Phys. Rev. B **45**, 9292 (1992).
[23] W. J. Antel, Jr., M. M. Schwickert, Tao Lin, W. L. O'Brien, and G. R. Harp, Phys. Rev. B (to be published 1 August 1999).
[24] S. D. Bader, D. Li, and Z. Q. Qiu, J. Appl. Phys. **76**, 6419 (1994).
[25] Tao Lin, M. A. Tomaz, M. M. Schwickert, and G. R. Harp, Phys. Rev. B **58**, 862 (1998).
[26] G. R. Harp, F. Perjeru, Tao Lin, M. M. Schwickert, W. J. Antel, Jr., M. A. Tomaz, and A. Anderson (unpublished).
[27] J. L. Erskine and E. A. Stern, Phys. Rev. B **12**, 5016 (1975).
[28] G. Schütz, W. Wagner, W. Wilhelm, P. Kienle, R. Zeller, R. Frahm, and G. Materlik, Phys. Rev. Lett. **58**, 737 (1987).
[29] Another way of determining magnetic moments is by the application of sum rules for the determination of the spin and orbital moments [P. Carra, B. T. Thole, M. Altarelli, and X. Wang, Phys. Rev. Lett. **70**, 694 (1993)]. By this method, the spin sum rule gives moment values quite similar to those obtained here. The present data is not of sufficient quality to reliably measure the orbital moment in these films.
[30] M. A. Tomaz, W. J. Antel, Jr., W. L. O'Brien, and G. R. Harp, Phys. Rev. B **55**, 3716 (1997).
[31] C. T. Chen, N. V. Smith, and F. Sette, Phys. Rev. B **43**, 6785 (1991).
[32] W. L. O'Brien and B. P. Tonner, Phys. Rev. B **51**, 617 (1995).
[33] M. G. Samant, J. Stöhr, S. S. P. Parkin, G. A. Held, B. D. Hermsmeier, F. Herman, M. van Schilfgaarde, L. C. Duda, D. C. Mancini, N. Wassdahl, and R. Nakajima, Phys. Rev. Lett. **72**, 1112 (1994).
[34] J. I. Lee, S. C. Hong, A. J. Freeman, and C. L. Fu, Phys. Rev. B **47**, 810 (1993).
[35] W. Keune, R. Halbauer, U. Gosner, J. Lauer, and D. L. Williamson, J. Appl. Phys. **48**, 2976 (1977); see, G. R. Harp, *Thin Films: Heteroepitaxial Systems* (World Scientific, Singapore, in press).
[36] J. Vogel, A. Fontaine, V. Cros, F. Petroff, J. P. Kappler, C. Krill, A. Rogalev, and J. Foulon, Phys. Rev. B **55**, 3663 (1997).
[37] K. Adachi, in *3d, 4d, and 5d Elements, Alloys, and Compounds*, edited by W. P. J. Wijn, Landolt-Börnstein, New Series, Group 3, Vol. 19, Pt. a (Springer-Verlag, Berlin, 1986).
[38] M. B. Stearns, Phys. Today **31** (4), 34 (1978).
[39] B. D. Cullity, *Introduction to Magnetic Materials* (Addison Wesley, Reading, MA, 1972), p. 148.
[40] S. Pizzini, A. Fontaine, E. Dartyge, C. Giorgetti, F. Baudelet, J. P. Kappler, P. Boher, and F. Giron, Phys. Rev. B **50**, 3779 (1994).